APPLIED SCIENCES AND ENGINEERING

Cell surface engineering with a pseudofibrotic ECM reprograms the antifibrotic activity of mesenchymal stromal cells

Xianghua Zhong[1]†, Xinchao Liu[1]†, Jiajia Luo[1]†, Xinyang Liu[1], Xueting Wei[1], Xi Peng[1], Lu Wang[2], Huaimin Wang[3], Kunyu Zhang[1,4,5]*, Liming Bian[1,4,5]*, Peng Shi[1,4,5]*

Fibrotic diseases, which impair tissue function and contribute to organ failure, remain a major clinical challenge with limited treatment options. Mesenchymal stromal cells (MSCs) offer promise for antifibrotic therapy via paracrine signaling, but their clinical efficacy is hindered by poor survival and limited functional activity after transplantation. Here, we present a cell surface engineering strategy that reprograms the antifibrotic function of MSCs by constructing a pseudofibrotic extracellular matrix (ECM) on their surface. Through in situ self-assembly of peptide-modified hyaluronic acid, we generate a nanofiber-based matrix that mimics the dense, disordered architecture of fibrotic ECM. This matrix activates the Piezo1/PI3K-Akt signaling pathway, inducing up-regulation of Mmp13—a key collagen-degrading matrix metalloproteinase—in engineered MSCs. In a rat model of myocardial infarction–associated fibrosis, engineered MSCs exhibit robust antifibrotic activity compared to unmodified MSCs. These findings establish a bioinspired strategy for MSC reprogramming and offer a path toward more effective cell-based therapies for fibrotic disease.

INTRODUCTION

Fibrosis is a progressive disorder marked by excessive extracellular matrix (ECM) deposition, which stiffens tissues, disrupts organ architecture, and drives chronic dysfunction or failure (1, 2). For instance, myocardial fibrosis substantially increases the risk of heart failure and arrhythmias, contributing to the estimated 17.9 million global cardiovascular deaths annually (3–5). Now, effective antifibrotic therapies are extremely limited. Mesenchymal stromal cell (MSC)–based therapies have recently emerged as a promising approach for treating fibrotic diseases, owing to their ability to modulate inflammation and remodel ECM via paracrine signaling (6–9). However, despite preclinical and clinical studies demonstrating the feasibility and safety of MSC-based interventions, the survival and functionality of in vitro–expanded MSCs posttransplantation remain exceedingly poor, leading to inconsistent clinical outcomes (10, 11).

To address these challenges, encapsulating MSCs within engineered matrices that provide cells with essential structural support and survival cues has emerged as a promising strategy to enhance therapeutic efficacy (12–14). Ideal matrices should have high porosity, excellent biocompatibility, appropriate mechanical properties, and the ability to modulate MSC functions tailored to the needs of specific disease contexts (15, 16). While extensive research has explored biomaterial-based approaches to provide appropriate matrix cues for guiding cellular behavior (17, 18), precise control over local matrix properties to direct MSC activity for resolving fibrotic injury remains a major challenge. More broadly, technologies that enable the customization of MSC-based therapeutics are urgently needed to achieve robust and predictable outcomes.

Fundamental studies have shown that excessive ECM deposition forms a dense, disordered fiber network that impairs cell migration and tissue repair (19, 20). In response, resident cells such as fibroblasts up-regulate matrix metalloproteinases (MMPs) to degrade pathological ECM in damaged tissue and promote regeneration (21–23). Inspired by this compensatory response, we hypothesized that engineering a fibrous matrix on the MSC surface, mimicking the fibrotic ECM, could similarly activate the antifibrotic capabilities of MSCs. To test this hypothesis, we constructed a nanofiber-based matrix on the surface of individual MSCs via biomolecular self-assembly. The matrix, composed of natural polysaccharides and peptides, replicates the dense, disordered fiber network while maintaining excellent biocompatibility. Notably, we found that this engineered microenvironment stimulates MSCs via the Piezo1/phosphatidylinositol 3-kinase (PI3K)-Akt signaling axis to up-regulate matrix metallopeptidase 13 (Mmp13), a critical collagenase involved in ECM remodeling. In a rat model of myocardial infarction (MI)–associated fibrosis, engineered MSCs demonstrated enhanced survival and potent antifibrotic activity compared to unmodified cells. Our work presents an innovative approach to reprogram MSC function through cell surface engineering, offering a promising strategy to optimize MSC-based therapies for fibrotic diseases.

[1]School of Biomedical Sciences and Engineering, South China University of Technology, Guangzhou International Campus, Guangzhou 511442, P. R. China. [2]Center of Cyclotron and PET Radiopharmaceuticals, Department of Nuclear Medicine and PET/CT-MRI Center, The First Affiliated Hospital of Jinan University, Guangzhou 510630, P. R. China. [3]Department of Chemistry, School of Science, Westlake University, Hangzhou 310024, P. R. China. [4]National Engineering Research Center for Tissue Restoration and Reconstruction, South China University of Technology, Guangzhou 510006, P. R. China. [5]Guangdong Provincial Key Laboratory of Biomedical Engineering, South China University of Technology, Guangzhou 510006, P. R. China.
*Corresponding author. Email: kyuzhang@scut.edu.cn (K.Z.); bianlm@scut.edu.cn (L.B.); pxs301@scut.edu.cn (P.S.)
†These authors contributed equally to this work.

RESULTS

Design and characterization of self-assembling peptide–modified hyaluronic acid

To construct a pseudofibrotic ECM on the surface of individual cells, we selected hyaluronic acid (HA), a natural ECM-derived polysaccharide, as the building block. We chemically modified HA with a

self-assembling peptide (NapFFKYp) to facilitate its assembly into a fibrous network that closely mimics the ECM structure (fig. S1 and Fig. 1A). Previous studies have shown that NapFFKYp is an enzyme-responsive self-assembling peptide composed of a (naphthalene-2-ly) acetyl group (Nap), two phenylalanine residues (Phe-Phe), a lysine (Lys), and a tyrosine phosphate moiety (pTyr) (24, 25). Upon dephosphorylation of pTyr by alkaline phosphatase (ALP), the Nap and Phe residues generate sufficient hydrophobic interactions to drive the self-assembly of the dephosphorylated substrate, NapFFKY, into nanofibrils in aqueous solution. This assembly process closely resembles the natural formation of collagen fibers, where the enzymatic cleavage of propeptides converts procollagens into collagen molecules that subsequently self-assemble into fibrils (26). As expected, we observed that HA conjugated with NapFFKYp (HA-NapFFKYp) self-assembled into nanofibrils in the presence of ALP, as evidenced by transmission electron microscopy (TEM) images (Fig. 1B). Circular dichroism spectroscopy further revealed that these nanofibrils adopted a β-sheet conformation (Fig. 1C), a characteristic secondary structure found in many ECM proteins. Upon the addition of ALP to HA-NapFFKYp solution, a transition from a liquid to gel state was observed (Fig. 1D). Rheological analysis demonstrated a substantial increase in the solution's modulus (Fig. 1E), indicating gel formation after enzymatic catalysis. The scanning electron microscopy (SEM) image clearly revealed that the gel matrix presented a porous, network-like structure (Fig. 1F). Collectively, these data demonstrate that HA-NapFFKYp self-assembles in aqueous solution to form a nanofiber-based matrix upon ALP-catalyzed dephosphorylation.

In situ self-assembly of HA-NapFFKYp forms a pseudofibrotic matrix on individual MSCs

We used HA-NapFFKYp to construct a pseudofibrotic matrix (pFM) on the surface of individual MSCs via enzyme-catalyzed in situ self-assembly. The HA motif binds to the CD44 receptor on MSCs, thereby anchoring HA-NapFFKYp to the cell surface (fig. S2). Upon ALP addition, HA-NapFFKYp undergoes dephosphorylation and subsequently self-assembles into a nanofiber-based matrix (Fig. 2A). We synthesized a series of HA-NapFFKYp variants with different grafting ratios of NapFFKYp and evaluated their cytocompatibility and mechanical strength (figs. S3 and S4). On the basis of these assessments, we selected HA-NapFFKYp with a 20% grafting ratio for subsequent experiments. Confocal fluorescence imaging confirmed effective surface anchoring of HA-NapFFKYp, as evidenced by the fluorescence colocalization of rhodamine B–labeled HA-NapFFKYp and the cell membrane dye 1,1′-dioctadecyl-3,3,3′,3′-tetramethylindodicarbocyanine, 4-chlorobenzenesulfonate salt (DiD). Furthermore, the presence of Congo Red staining, which specifically binds to nanofibrils with a β-sheet conformation, indicated that HA-NapFFKYp successfully self-assembled into nanofibrils on the MSC surface following ALP treatment (Fig. 2B and fig. S5). These findings were corroborated by SEM imaging, which revealed the formation of a three-dimensional, fibrous network surrounding MSCs (Fig. 2C). Flow cytometry further demonstrated that the single-cell modification achieved an efficiency of 99.5% (Fig. 2D).

We next investigated the effect of HA-NapFFKYp gelling concentration on the thickness, mechanical properties, and pore size of the pFM, as these factors directly influence the viability and
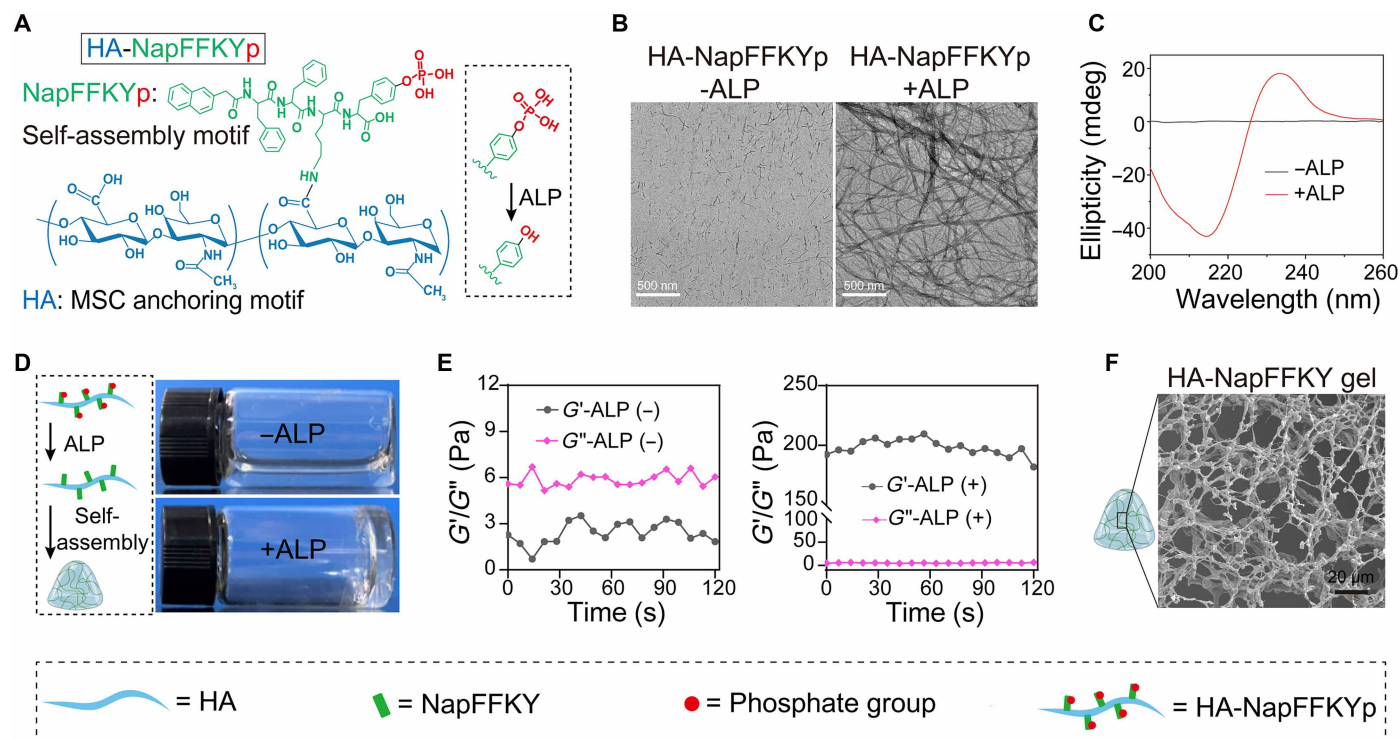

Fig. 1. Synthesis and characterization of self-assembled HA-NapFFKYp. (**A**) Schematic illustration showing the structure and dephosphorylation mechanism of HA-NapFFKYp. (**B**) Representative TEM images of HA-NapFFKYp before and after ALP addition. (**C**) Circular dichroism spectra of HA-NapFFKYp in the absence and presence of ALP. (**D**) Optical images of HA-NapFFKYp solution in the absence or presence of ALP. (**E**) Rheology tests of HA-NapFFKYp in the absence or presence of ALP. (**F**) Representative SEM image of the gel matrix formed by HA-NapFFKYp after ALP addition.
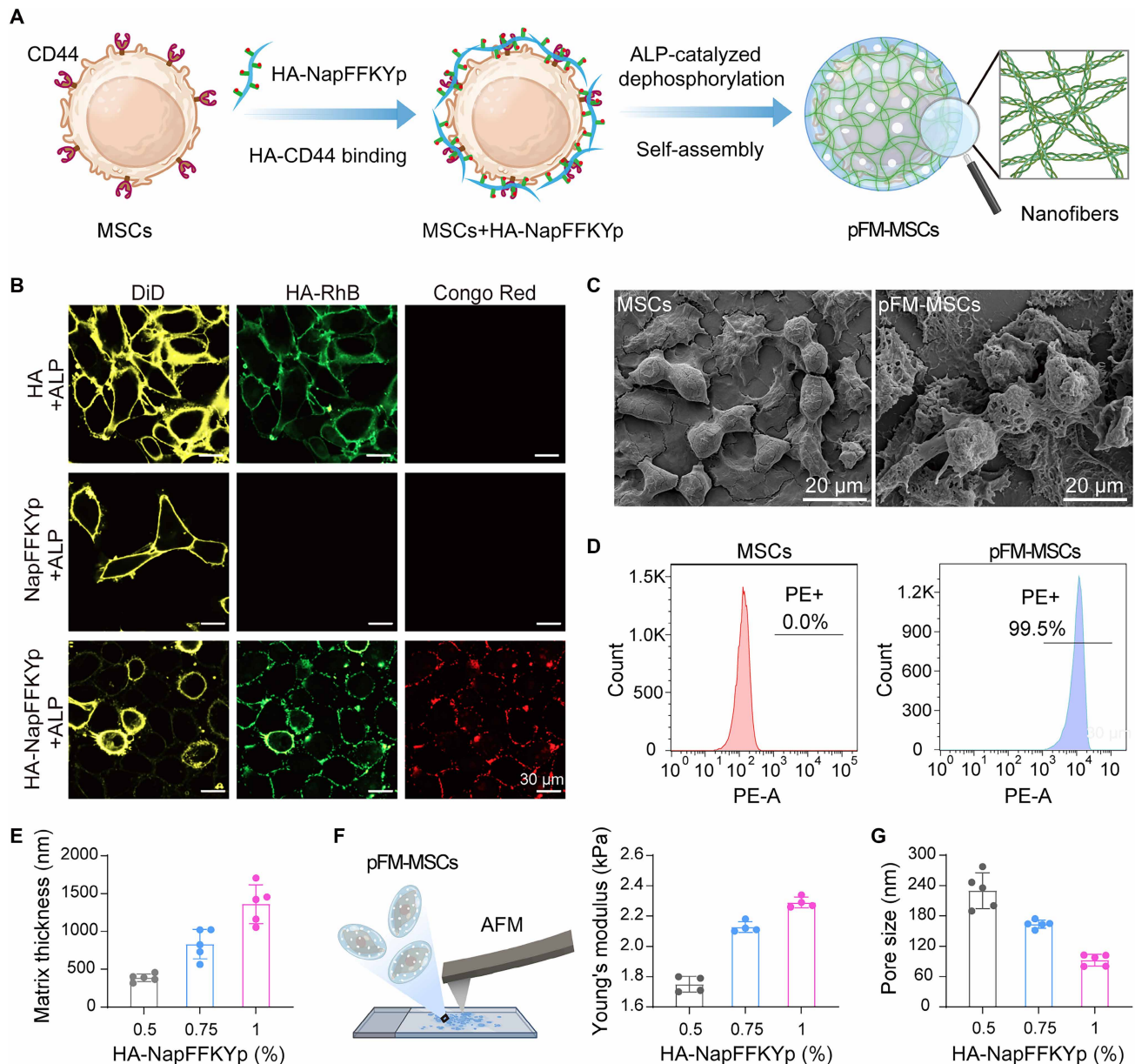
Fig. 2. Preparation and characterization of pFM on individual MSC surfaces. (**A**) Schematic illustration of HA-NapFFKYp physically adsorbed onto the MSC surface, followed by self-assembly into a nanofiber-based matrix upon dephosphorylation. (**B**) Representative confocal images of pFM-MSCs. Cell membranes were stained with DiD, the HA motif was labeled with rhodamine B (RhB), and nanofibrils were stained with Congo Red. (**C**) Representative SEM images of MSCs and pFM-MSCs. (**D**) Flow cytometry analysis showing the proportion of singly encapsulated MSCs. (**E**) Matrix thickness on individual MSC surfaces at varying concentrations of HA-NapFFKYp. Data are presented as the means $\pm$ SD ($n = 5$). (**F**) Mechanical properties of encapsulated MSCs at varying concentrations of HA-NapFFKYp. Data are presented as the means $\pm$ SD ($n = 4$). (**G**) Pore size of the matrix on individual MSC surfaces at varying concentrations of HA-NapFFKYp. Data are presented as the means $\pm$ SD ($n = 5$).

biological function of encapsulated MSCs. As the HA-NapFFKYp concentration increased, both the matrix thickness and mechanical strength increased, whereas the pore size decreased correspondingly (Fig. 2, E to G, and fig. S6). At a concentration of 1%, the thickness of the matrix was around 1400 nm and the mechanical strength of encapsulated cells reached 2.3 kPa, but the pore size reduced to 90 nm, potentially hindering the release of therapeutic components such as exosomes (30 to 150 nm) (27, 28). Moreover, HA-NapFFKYp at a concentration of 1% exhibited some cytotoxicity (fig. S7). In contrast, at a concentration of 0.75%, the pFM maintained an optimal balance of structural properties, with a pore size of 165 nm, a thickness of 830 nm, and a mechanical strength of 2.1 kPa. This porous three-dimensional network did not impede the release of paracrine factors from MSCs (fig. S8), and the viability of encapsulated cells remained high. On the basis of these findings, we selected 0.75% HA-NapFFKYp for MSC encapsulation, providing a pFM with optimal cytocompatibility, fibrous network, and therapeutic widow.

pFM protects MSCs from the harsh pathological microenvironment

The harsh pathological microenvironment of injured tissues—characterized by hypoxia, excessive reactive oxygen species (ROS), and inflammatory cytokine storms—can severely damage transplanted cells in cell therapy. A biomimetic matrix is expected to provide a protective barrier, shielding MSCs from these hostile conditions (Fig. 3A). Our results demonstrated that pFM-coated MSCs (pFM-MSCs) exhibited substantially greater resistance to pathological stressors compared to bare MSCs under $Na_2S_2O_4$-induced hypoxia, H_2O_2-induced oxidative stress, and tumor necrosis factor–α (TNF-α)–induced inflammation. Specifically, at concentrations of 6 mM $Na_2S_2O_4$, 1.2 mM H_2O_2, and TNF-α (100 ng/ml), the viabilities of pFM-MSCs were 21.3, 22.3, and 72.6%, respectively, whereas bare MSCs exhibited substantially lower viabilities of 11.2, 9.6, and 45.9% (Fig. 3, B to D). Furthermore, the pFM effectively mitigated shear-induced damage to MSCs during centrifugation, simulating the mechanical stress encountered during cell injection (Fig. 3E). Collectively, these results

indicate that the biomimetic matrix substantially enhances MSC survival in pathological microenvironments.

To further investigate the mechanism underlying this protective effect, we cultured pFM-MSCs and MSCs in a TNF-α–rich microenvironment and performed transcriptomic analysis. A volcano plot revealed that 3382 differentially expressed genes (DEGs) were upregulated and 3704 DEGs were down-regulated in pFM-MSCs compared to MSCs (Fig. 3F). Notably, under TNF-α stimulation, pFM-MSCs exhibited higher levels of antiapoptotic gene expression and lower levels of proapoptotic gene expression than uncoated MSCs (Fig. 3G and fig. S9), primarily due to the pFM physically blocking TNF-α from binding to TNF receptors on the MSC surface, thereby inhibiting TNF signaling–mediated apoptosis (29). In addition, Gene Ontology (GO) enrichment analysis was performed on DEGs, revealing several key GO terms, such as "negative regulation of apoptosis process," "positive regulation of cell population proliferation," and "positive regulation of gene expression" being notably enriched (Fig. 3H). These findings suggest that the biomimetic matrix
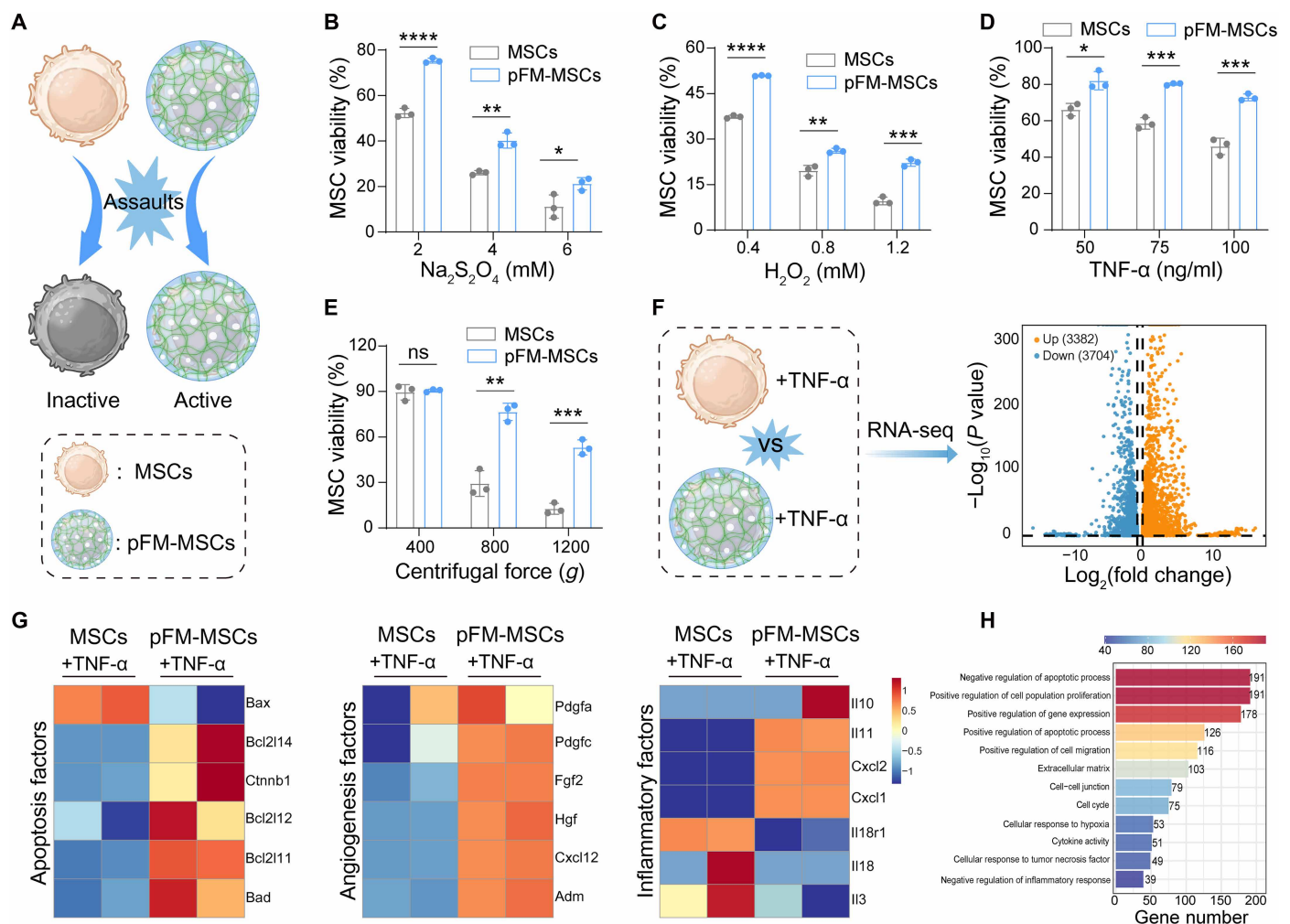

Fig. 3. Cytoprotective effects of pFM for MSCs. (**A**) Schematic comparison of bare MSCs and pFM-MSCs when exposed to environmental assaults. (**B** to **E**) Cell viability of MSCs and pFM-MSCs after exposure to different concentrations of $Na_2S_2O_4$ (B), H_2O_2 (C), and TNF-α (D), as well as to different centrifugal forces (E). Data are presented as the means ± SD ($n = 3$). (**F**) Volcano plot showing DEGs between MSCs and pFM-MSCs under TNF-α mimetic inflammatory conditions. (**G**) Heatmap illustrating DEGs associated with apoptosis, angiogenesis, and inflammation. (**H**) GO enrichment analysis showing the 12 most notably enriched biological process terms. Statistical analysis was performed using a one-way ANOVA followed by Tukey's multiple comparisons test (*$P < 0.05$; **$P < 0.01$; ***$P < 0.001$; ****$P < 0.0001$; ns, nonsignificant).

helps maintain the therapeutic functionality of MSCs and enhances antiapoptotic gene expression, thereby promoting MSC survival in the inflammatory microenvironment.

pFM enhances Mmp13 production via activation of the Piezo1/PI3K-Akt pathway

The primary objective of this study was to investigate whether a nanofiber-based matrix on the MSC surface—designed to mimic the fibrotic ECM—could activate MSCs' antifibrotic programs, particularly through the compensatory up-regulation of MMPs. To this end, we performed RNA sequencing (RNA-seq) on pFM-MSCs and bare MSCs to compare the expression of paracrine-associated genes. The results revealed notable up-regulation of genes involved in ECM degradation, including *Mmp3*, *Mmp10*, *Mmp13*, and *Mmp17*, along with down-regulation of genes associated with collagen synthesis (Fig. 4, A and B, and fig. S10). Notably, *Mmp13* showed the most pronounced up-regulation among all paracrine-related genes (fig. S11). The *Mmp13* up-regulation in pFM-MSCs was further validated by quantitative polymerase chain reaction (qPCR), enzyme-linked immunosorbent assay (ELISA), and Western blot analyses (Fig. 4, C to E). To determine whether this up-regulation was specifically driven by the fibrous structure, we included two control groups: one in which HA-NapFFKYp was bound onto the MSC surface without forming nanofibers and another in which dopamine-modified HA was covalently cross-linked to form a nonfibrous gel (fig. S12). qPCR analysis demonstrated that *Mmp13* up-regulation occurred exclusively in the presence of pFM, underscoring the importance of the fibrous structure in eliciting this antifibrotic response (Fig. 4F).

Given the strong up-regulation of *Mmp13*, we further explored the underlying mechanism. Kyoto Encyclopedia of Genes and Genomes (KEGG) enrichment analysis of up-regulated DEGs revealed notable enrichment in the fluid shear stress and calcium signaling pathway (Fig. 4G), suggesting that *Mmp13* up-regulation may be driven by mechanical signals mediated by mechanosensitive channels on the MSC surface. We thus analyzed major mechanosensitive channels and observed that pFM-MSCs exhibited increased expression of *Piezo1* (Fig. 4, H and I). Recent studies have demonstrated that Piezo1 activation induces Ca^{2+} influx, converting mechanical cues into biochemical signals that regulate MMP expression (*30–33*). We thus hypothesized that Piezo1 activation triggered by the nanofiber-based matrix was responsible for Mmp13 up-regulation. To verify our hypothesis, we treated MSCs with the Piezo1-specific agonist Yoda1 and the Piezo1-specific inhibitor GsMTx4, followed by assessments of intracellular Ca^{2+} levels and Mmp13 expression. Both Yoda1 and pFM substantially increased intracellular Ca^{2+} levels in MSCs, whereas GsMTx4 reduced Ca^{2+} levels in pFM-MSCs (Fig. 4, J and K). Furthermore, inhibition of Piezo1 suppressed the up-regulation of Mmp13 expression in pFM-MSCs (Fig. 4, L and M). These results solidly demonstrate that the nanofiber-based matrix enhances Mmp13 production by activating Piezo1. To further determine whether HA-CD44 binding cooperates with Piezo1 to regulate Mmp13 expression, we performed qPCR experiments using a CD44 blocking antibody in the presence of either Yoda1 or GsMTx4, followed by assessment of *Mmp13* expression. The results showed that *Mmp13* expression depended exclusively on the activation state of Piezo1 and was unaffected by HA-CD44 binding (fig. S13).

Next, we investigated the downstream signaling pathway by which Piezo1 activation promotes Mmp13 expression. KEGG enrichment analysis identified the PI3K-AKT signaling pathway as notably enriched

(Fig. 4G), suggesting its potential role in regulating Mmp13 expression. Our data revealed that Yoda1 and pFM increased phosphorylated AKT (p-AKT) levels without affecting total AKT levels, while GsMTx4 inhibited AKT phosphorylation in pFM-MSCs (Fig. 4N). Moreover, administration of the PI3K inhibitor LY294002 attenuated Mmp13 up-regulation (Fig. 4O and fig. S14), confirming that Piezo1 activation promotes Mmp13 expression via the PI3K-AKT signaling pathway. Collectively, these results demonstrate that pFM enhances Mmp13 production in MSCs through the Piezo1/PI3K-AKT signaling axis. A schematic summary of this mechanism is illustrated in Fig. 5.

To evaluate the functional implications of Mmp13 up-regulation, we investigated whether pFM-MSCs could degrade collagen in a paracrine manner, potentially facilitating matrix remodeling and fibrosis reversal. Coculturing pFM-MSCs with a collagen matrix revealed progressive collagen degradation, as evidenced by Ponceau S staining. The formation of pits at the matrix edges and inward penetration of degradation substantially reduced collagen content, as indicated by decreased staining intensity (fig. S15). In addition, knockdown of *Mmp13* notably reduced the collagen degradation efficiency of pFM-MSCs (fig. S16). These findings suggest that pFM-MSCs have collagen-degrading capacity, highlighting their potential to reverse tissue fibrosis.

pFM-MSCs suppress cardiac fibrosis progression in vivo

Encouraged by the enhanced survival and collagen degradation capacity of pFM-MSCs in vitro, we further evaluated their viability and antifibrotic effect in a rat model of MI with fibrosis (Fig. 6A). We first established the MI model (fig. S17) and injected luciferase-expressing MSCs into the heart. The survival of MSCs was monitored in real time using the IVIS Lumina II system. Bioluminescence imaging revealed that the heart bioluminescence intensity (BLI) in the pFM-MSC group was notably higher than that in the MSC-only group throughout the monitoring period. Moreover, the bioluminescence signal persisted longer in the pFM-MSC group (Fig. 6, B and C). By day 7, the MSC group showed almost no detectable bioluminescence signal in the heart region, whereas the pFM-MSC group retained a strong signal. Quantitative analysis indicated that BLI in the heart region of the pFM-MSC group was 11 times higher than that of the MSC group, demonstrating that pFM substantially improved MSC survival in the myocardium. In addition, we labeled pFM with the fluorescent dye Cy5 and then injected Cy5-pFM-MSCs into the heart to evaluate the in vivo fate of pFM. In vivo fluorescence imaging revealed a gradual decrease in Cy5 signal over time, which became very weak by day 5, indicating that pFM undergoes progressive degradation and does not persist in a long term (fig. S18).

To assess the antifibrotic potential of pFM-MSCs in vivo, we monitored cardiac fibrosis progression in real time using positron emission tomography/computed tomography (PET/CT) imaging, with the ^{18}F-labeled fibroblast activation protein inhibitor (^{18}F-FAPI) as a radiotracer specifically targeting cardiac myofibroblasts (Fig. 6D). On day 7, myocardial ^{18}F-FAPI uptake peaked across all groups, reflecting severe injury and fibrosis, consistent with a previous report indicating that ^{18}F-FAPI levels peak around day 7 following heart injury (*34*). From this point, myocardial ^{18}F-FAPI uptake gradually declined, with the most rapid reduction observed in the pFM-MSC group. By days 14 and 28, the ^{18}F-FAPI signal in the pFM-MSC group had decreased to 71 and 37% of the day 7 level, respectively, which was notably lower

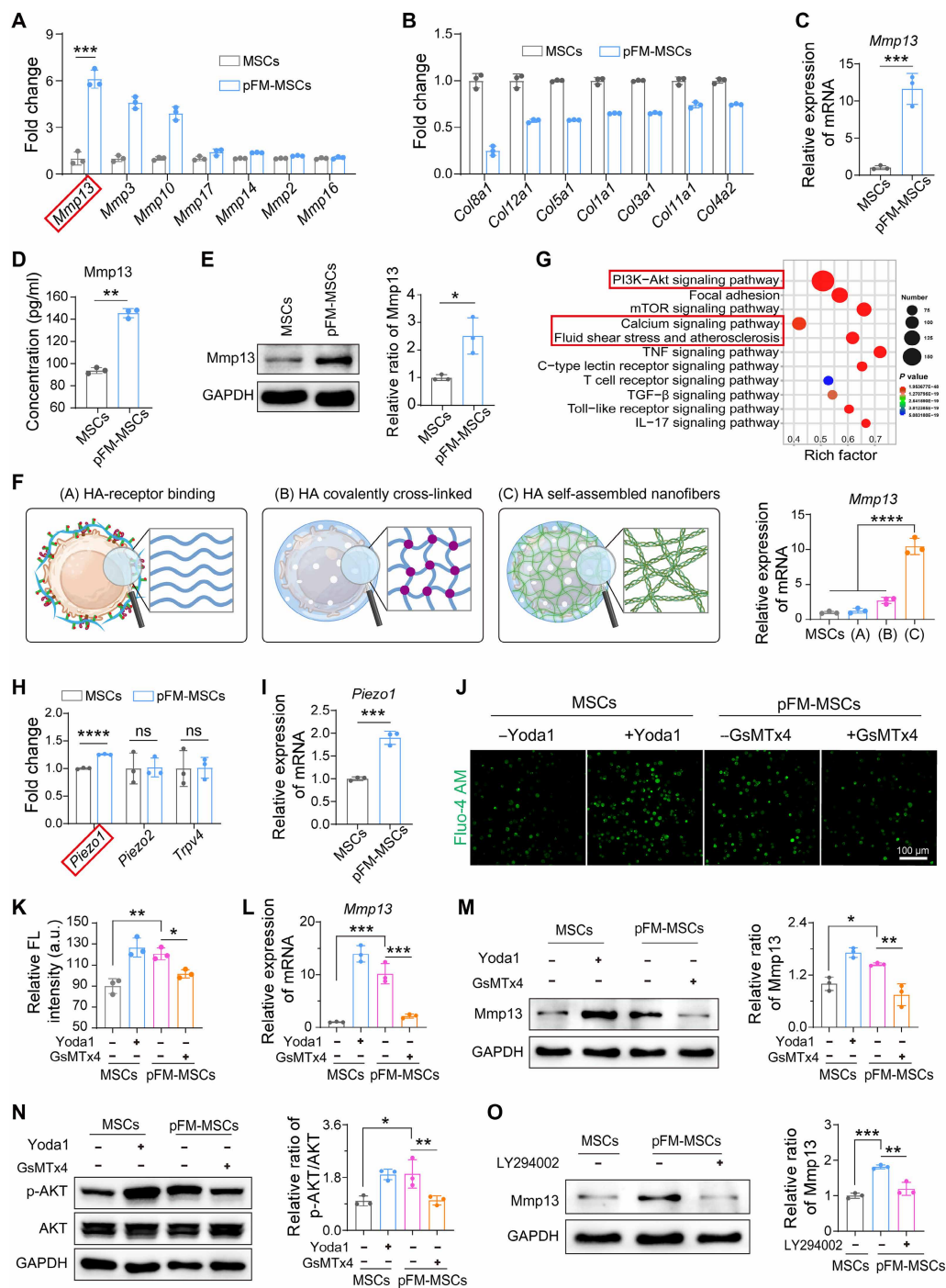**Fig. 4. Mechanistic investigation of Mmp13 up-regulation in pFM-MSCs.** (**A** and **B**) Quantification of gene expression related to ECM remodeling (A) and collagen synthesis (B) in MSCs and pFM-MSCs, as measured by RNA sequencing. (**C**) Quantification of *Mmp13* gene expression in MSCs and pFM-MSCs, as determined by qPCR. (**D**) Quantification of Mmp13 secretion in MSCs and pFM-MSCs by ELISA. (**E**) Protein expression levels of Mmp13 in MSCs and pFM-MSCs. (**F**) Schematic illustration of HA-receptor binding, HA covalently cross-linked, and HA self-assembled into nanofibers, along with quantification of *Mmp13* gene expression. (**G**) KEGG pathway enrichment analysis of DEGs. (**H**) Quantification of mechanosensitive channel gene expression in MSCs and pFM-MSCs, as measured by RNA sequencing. (**I**) Quantification of *Piezo1* gene expression in MSCs and pFM-MSCs, as determined by qPCR. (**J**) Representative confocal images showing intracellular calcium ions in MSCs after different treatments. (**K**) Quantification of the fluorescence (FL) intensity of intracellular calcium ions shown in (J). a.u., arbitrary units. (**L**) Quantification of *Mmp13* gene expression in MSCs after different treatments, as determined by qPCR. (**M**) Mmp13 protein expression levels in MSCs and pFM-MSCs in the absence and presence of Yoda1 and GsMTx4. (**N**) Phosphorylated AKT (p-AKT) protein expression levels in MSCs and pFM-MSCs in the absence and presence of Yoda1 and GsMTx4. (**O**) Mmp13 protein expression levels in MSCs and pFM-MSCs in the absence and presence of LY294002 (25 μM). For (A) to (F), (H), (I), and (K) to (O), data are presented as the means ± SD ($n = 3$). Statistical analysis was performed using a one-way ANOVA followed by Tukey's multiple comparisons test (*$P < 0.05$; **$P < 0.01$; ***$P < 0.001$; ****$P < 0.0001$).
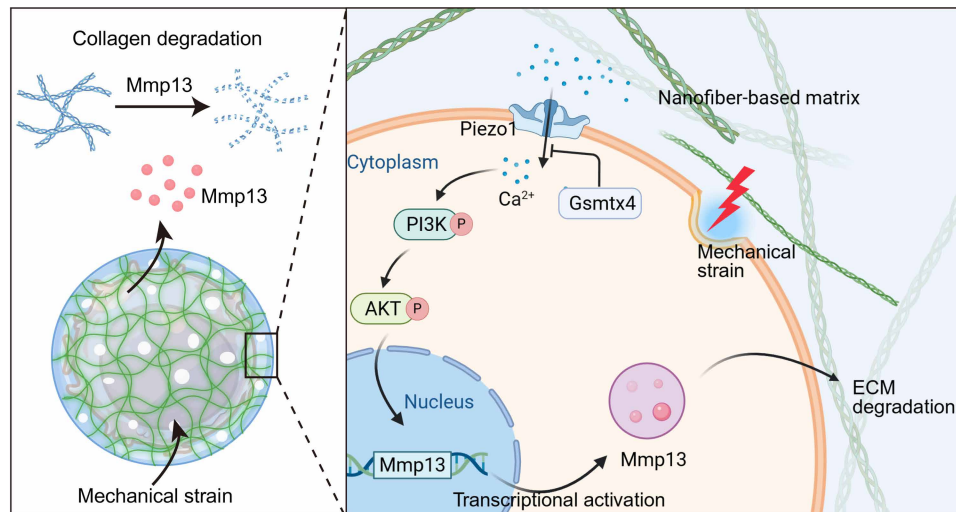
Fig. 5. Schematic illustration of the mechanism by which the nanofiber-based matrix enhances Mmp13 production in MSCs. This schematic outlines the signaling pathway by which the nanofiber-based matrix up-regulates Mmp13 expression in MSCs.

than that in both the phosphate-buffered saline (PBS) and MSC groups (Fig. 6E). These results demonstrate that pFM-MSCs provide superior therapeutic effects in alleviating myocardial fibrosis.

Histological analysis of heart tissues 4 weeks postinjection further confirmed the antifibrotic effects of pFM-MSCs. Masson's trichrome and Sirius Red staining revealed reduced fibrotic mass and improved preservation of normal myocardium in the pFM-MSC group compared to the other treatment groups, including the *Mmp13*-knockdown pFM-MSC group (Fig. 6, F and G, and figs. S19 and S20). In addition, the total hydroxyproline content—a key marker of collagen—was substantially reduced in the pFM-MSC group, reaching levels comparable to those in the sham group (Fig. 6H), suggesting that pFM-MSCs effectively reduce collagen content in myocardial tissues. Given that myocardial fibrosis increases tissue stiffness, thereby impairing cardiac contractility and diastolic function (*35*), we evaluated whether pFM-MSCs could help maintain physiological heart tissue stiffness. Atomic force microscopy was used to analyze the microelasticity of heart sections. The results demonstrated that treatment with pFM-MSCs substantially reduced heart tissue stiffness, effectively restoring it to near-physiological levels (Fig. 6I). The reduction in fibrosis, as evidenced by diminished ^{18}F-FAPI uptake, decreased collagen deposition, lower hydroxyproline levels, and restored tissue elasticity, can be attributed to elevated Mmp13 secretion from pFM-MSCs. MMPs degrade excessive ECM, releasing matrix-bound cytokines and generating bioactive fragments that recruit immune cells and modulate inflammation, ultimately promoting ECM remodeling and tissue repair (Fig. 6J) (*36–39*). Together, these findings establish cell surface engineering with a nanofiber-based matrix as a potent strategy to boost MSC survival and antifibrotic activity in MI.

pFM augments the therapeutic efficacy of MSCs in restoring cardiac function

We further examined whether pFM-MSCs could effectively restore cardiac function. pFM-MSCs or MSCs were delivered via intramyocardial injection, and cardiac function was evaluated using echocardiography after 28 days (Fig. 7, A and B). Compared to the PBS group, the MSC-only treatment improved the left ventricular ejection

fraction (LVEF) from 32 to 53% and the left ventricular fractional shortening (LVFS) from 16 to 28%. In contrast, treatment with pFM-MSCs resulted in a more notable improvement, with LVEF increasing from 32 to 68% and LVFS increasing from 16% to 40% (Fig. 7C), and cardiac contractile function was also superior in the pFM-MSC group compared to the other groups (fig. S21), indicating that pFM-MSCs provided the most effective recovery of cardiac function. Notably, knockdown of *Mmp13* markedly attenuated the reparative effect of pFM-MSCs on cardiac function, indicating a critical role of Mmp13 in mediating heart function recovery (fig. S22). We also assessed left ventricular hypertrophy by measuring the left ventricular end-diastolic volume and left ventricular mass. Specifically, the left ventricular end-diastolic volume (LVEDV) in the pFM-MSC group was 289 ± 14 μl, closest to the sham group (218 ± 10 μl) and notably lower than the PBS group (455 ± 17 μl) and the MSC group (365 ± 14 μl), indicating that pFM-MSC treatment effectively attenuated pathological left ventricular dilation and hypertrophy (Fig. 7D). The enhanced therapeutic benefits observed in the pFM-MSC group can be attributed to the markedly improved survival and antifibrotic effects conferred by pFM encapsulation.

We also verified the therapeutic effect of pFM-MSCs by histological examination. Hematoxylin-eosin (H&E) staining revealed severe inflammatory cell infiltration in the injured myocardial tissue of the PBS group. While MSC treatment alleviated inflammation to some extent, administration of pFM-MSCs resulted in a more pronounced restoration of the injured myocardium, suggesting a notable anti-inflammatory effect (Fig. 7E). To investigate neovascularization, we performed immunofluorescence staining for α-smooth muscle actin (α-SMA) and CD31, which mark vascular structures. The CD31^{+} vessel density in the MSC group increased by ~1.3-fold relative to the PBS group, while the pFM-MSC group showed a ~1.7-fold increase compared with the PBS group (Fig. 7F). Similarly, the α-SMA[+] vessel density in the MSC group increased by ~1.5-fold compared with PBS, whereas the pFM-MSC group exhibited a ~1.9-fold increase relative to the PBS group (Fig. 7G). These results clearly demonstrate that pFM-MSCs exert a stronger proangiogenic effect than MSCs. Collectively, these results demonstrate that pFM-MSCs provide the
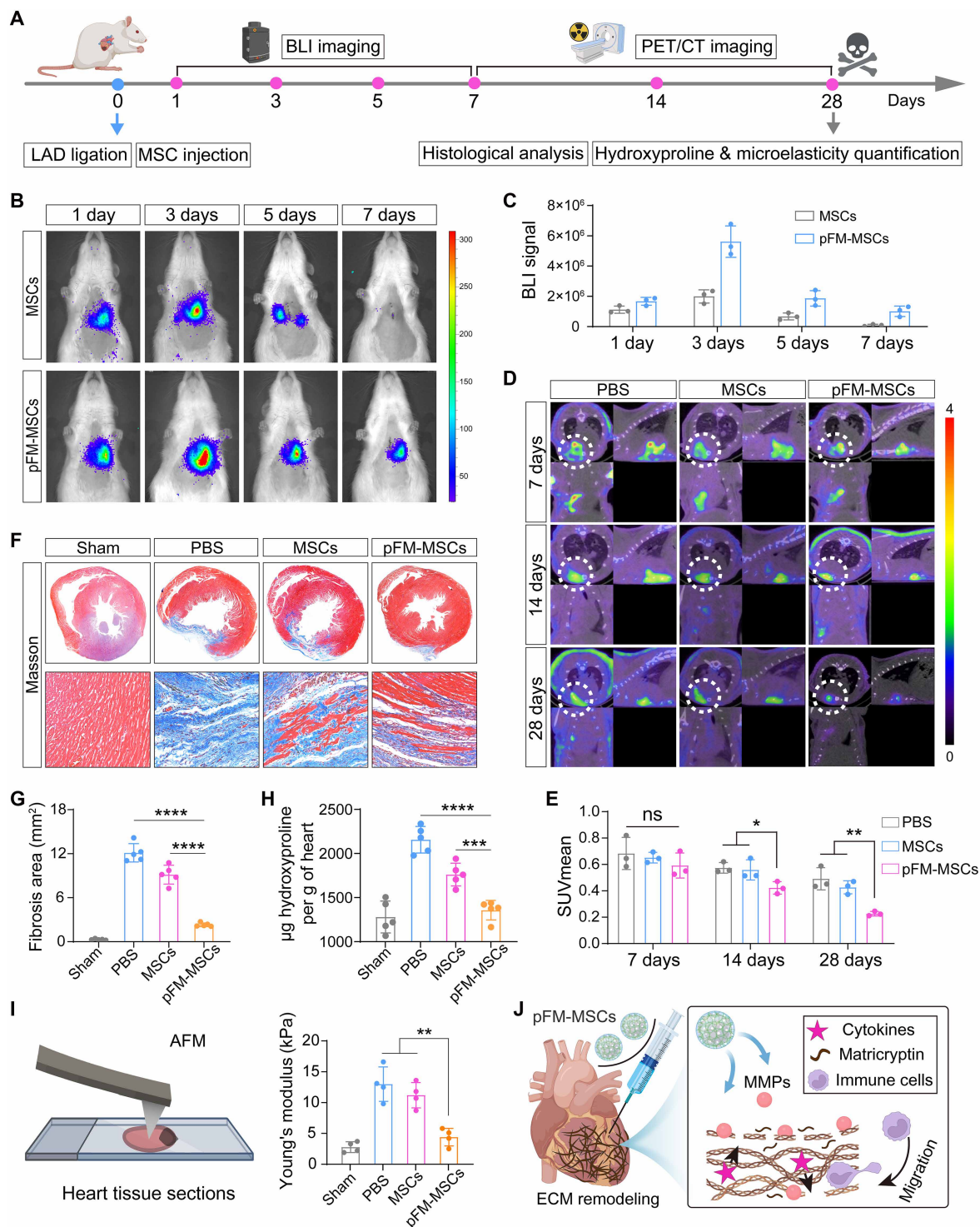
Fig. 6. Survival and antifibrotic effects of pFM-MSCs in fibrotic rat hearts. (**A**) Schematic illustration showing the timeline of the in vivo study. (**B**) Representative bioluminescence images illustrating the surviving MSCs within injured hearts at the indicated time points. (**C**) Quantitative analysis of BLI signals in the MSC and pFM-MSC groups. Data are presented as the means ± SD ($n = 3$). (**D**) Representative ^{18}F-FAPI PET/CT images of different treatment groups at the indicated time points. (**E**) Quantitative analysis of ^{18}F-FAPI uptake in different treatment groups at the indicated time points. Data are presented as the means ± SD ($n = 3$). SUVmean, mean standardized uptake value. (**F**) Representative images of Masson's trichrome–stained cardiac sections 4 weeks after fibrotic injury. Blue indicates fibrotic tissue; red indicates viable myocardium. (**G**) Quantitative analysis of fibrotic area in different groups. Data are presented as the means ± SD ($n = 5$). (**H**) Hydroxyproline levels in heart tissues. Data are presented as the means ± SD ($n = 5$). (**I**) Microelasticity of heart tissue sections measured by atomic force microscopy. Data are presented as the means ± SD ($n = 4$). (**J**) Schematic illustration of MMP-mediated ECM remodeling and tissue repair. Statistical analysis was performed using a one-way ANOVA followed by Tukey's multiple comparisons test (*$P < 0.05$; **$P < 0.01$; ***$P < 0.001$; ****$P < 0.0001$).
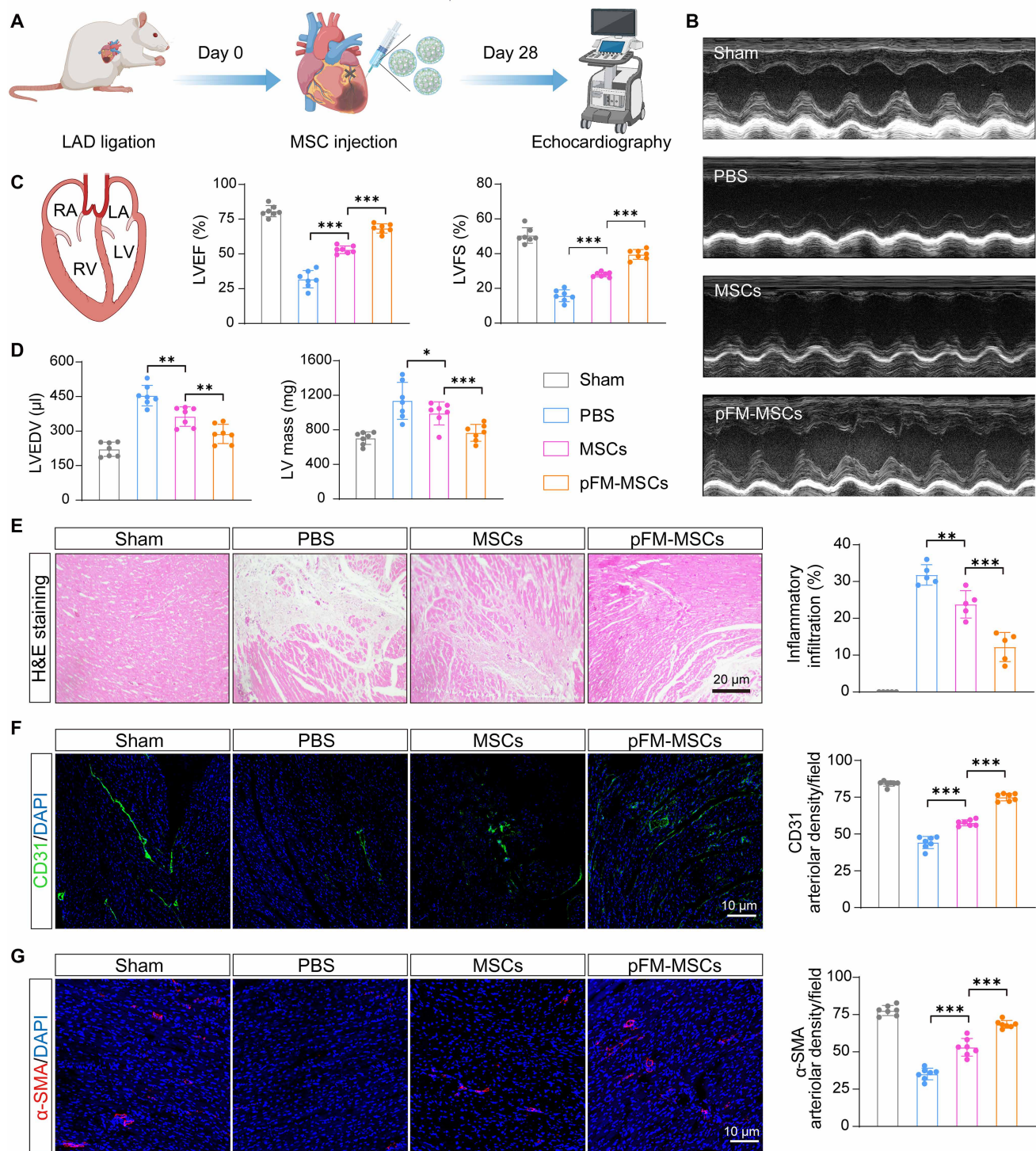
Fig. 7. Restoration of cardiac function in rats following treatment with pFM-MSCs. (**A**) Schematic illustration of the intramyocardial delivery of pFM-MSCs for the treatment of myocardial injury. (**B**) Representative echocardiographic images showing left ventricle wall motion 4 weeks after different treatments. (**C**) Schematic diagram of rat heart anatomy and quantitative analysis of LVEF and LVFS measured by echocardiography. RA, right atrium; LA, left atrium; RV, right ventricle; LV, left ventricle. Data are presented as the means ± SD ($n = 7$). (**D**) Quantitative analysis of LV volume and LV mass measured by echocardiography. Data are presented as the means ± SD ($n = 7$). (**E**) Representative H&E-stained images following various treatments and quantification of inflammatory cell infiltration. Data are presented as the means ± SD ($n = 5$). (**F**) Representative immunofluorescence images of CD31 staining and quantification of CD31$^+$ vasculature. Data are presented as the means ± SD ($n = 7$). (**G**) Representative immunofluorescence images of α-SMA staining and quantification of α-SMA$^+$ vasculature. Data are presented as the means ± SD ($n = 7$). Statistical analysis was performed using a one-way ANOVA followed by Tukey's multiple comparisons test (*$P < 0.05$; **$P < 0.01$; ***$P < 0.001$).

most substantial therapeutic benefit for injured hearts. Last, hematology examination and H&E staining of major organs confirmed that pFM-MSCs exhibited excellent biosafety, with no signs of systemic toxicity (figs. S23 and S24).

DISCUSSION

Engineering a biomimetic ECM at the single-cell level with tunable matrix properties offers an effective strategy for tailoring MSC-based therapies. Compared to bulk hydrogel encapsulation, providing a uniform matrix for each single cell offers several distinct advantages. First, it enables precise control over the cellular microenvironment, enhancing cell functionality. Second, it improves mass transport, facilitating efficient oxygen and nutrient diffusion while preventing waste accumulation around individual cells (40, 41). Last, cell surface engineering allows for greater flexibility in in vivo delivery, enabling administration through various routes to optimize therapeutic outcomes. In this study, we constructed a nanofiber-based matrix on the surface of individual MSCs via biomolecular self-assembly. We demonstrate that this engineered matrix improves MSC survival in the pathological microenvironment. Notably, our findings reveal that the nanofiber-based matrix uniquely enhances the antifibrotic potential of MSCs by promoting Mmp13 expression through the structural mimicry of the fibrotic ECM.

Previous studies have shown that MSCs encapsulated in soft microgels can sense mechanical cues through integrin-RGD (arginylglycylaspartic acid) interactions, thereby activating downstream signaling pathways such as focal adhesion kinase, Src, and mitogen-activated protein kinase to regulate cellular functions (42–44). Our findings reveal that the nanofiber-based matrix activates Piezo1 to regulate cellular functions. Piezo1, a mechanosensitive ion channel, responds to membrane tension and transduces mechanical stimuli into biochemical signals that influence cellular functions (45, 46). Prior research has shown that in nanofiber-rich microenvironments, cells can respond to physical stimuli via Piezo1 activation (47). In this study, peptide-modified HA binds to the MSC surface and undergoes in situ self-assembly to form nanofibrils. We speculate that this in situ nanofibril formation imposes mechanical constraints or induces membrane stretching, thereby triggering Piezo1 activation. This mechanism differs from classical integrin-mediated signaling, highlighting a different pathway by which the nanofiber-based matrix modulates the MSC function.

It is also important to highlight that we introduce a cell surface engineering technology based on molecular self-assembly, which offers several advantages over the widely used microfluidic-based single-cell encapsulation strategy (42, 48, 49). First, the engineering process is simple and efficient, requiring only the mixing of cells with biomaterials under physiological conditions for a few hours, without the need for specialized equipment, substantially reducing preparation complexity and manufacturing costs. Second, unlike microfluidic-based encapsulation, which follows a Poisson distribution, our self-assembly–based approach achieves an engineering efficiency of up to 99.5%, ensuring uniformity across encapsulated cells. Third, the process does not involve harsh chemical reagents, and cells are not exposed to shear stress, preserving high cell viability. Last, the scalability of this method is not constrained by specialized equipment, allowing for large-scale and high-throughput preparation of engineered cells, which is crucial for advancing clinical applications. Collectively, this study presents an innovative strategy

and scientific foundation for optimizing MSC-based therapies, with notable implications for regenerative medicine.

MATERIALS AND METHODS
Study design

The primary objective of this study was to construct a nanofiber-based matrix on the MSC surface—designed to mimic the fibrotic ECM—to enhance the survival of MSCs and activate their antifibrotic programs. The study objectives were finished by (i) designing and characterizing self-assembling peptide–modified HA, (ii) constructing and characterizing pseudofibrotic ECM (pFM)–encapsulated individual MSCs, (iii) investigating cytoprotective effects of pFM for MSCs in the harsh pathological microenvironment, (iv) investigating the antifibrotic activity of MSCs in vitro and exploring the underlying mechanism, and (v) evaluating the survival, antifibrotic effect, and therapeutic efficacy of pFM-MSCs in vivo. For animal experiments, rats were randomly assigned to various groups. No animals were excluded from the in vivo experiments. The sample sizes of the experimental groups were determined on the basis of previous reports and calculations. Detailed information on the number of replicates, statistical tests used, and corresponding P values are provided in the figure legends.

Materials

The self-assembling peptide (NapFFKYp) was synthesized by Sangon Biotech Co., Ltd. (Shanghai, China). HA was purchased from Shanghai Macklin Biochemical Co., Ltd. ALP was obtained from Sigma-Aldrich. The DiD cell-labeling solution and Cell Counting Kit-8 (CCK-8) were purchased from Beyotime Biotechnology Co., Ltd. (Shanghai, China). The anti-MMP13 antibody (catalog no. ab39012) was purchased from Abcam. FITC (fluorescein isothiocyanate) anti-mouse CD31 (catalog no. 102506) was purchased from BioLegend. Anti-rat α-SMA (catalog no. 14-9760-80) was purchased from Invitrogen. The Phospho-Akt (Ser^{473}) (D9E) XP Rabbit monoclonal antibody (catalog no. 4060) and Akt (pan) (C67E7) Rabbit monoclonal antibody (catalog no. 4691) were purchased from Cell Signaling Technology. The GAPDH (glyceraldehyde-3-phosphate dehydrogenase) monoclonal antibody (catalog no. 60004-1-Ig) was obtained from Proteintech. Masson's trichrome staining kit and Modified Sirius Red staining kit were purchased from Solarbio (Beijing, China). The ELISA kits were from Shanghai Enzyme-linked Biotechnology Co., Ltd.

Synthesis of HA-NapFFKYp

Fifty milligrams of HA (0.124 mmol) was dissolved in 15 ml of formamide with magnetic stirring at 50°C until a clear solution was obtained. Subsequently, 56.6 mg of *O*-(7-azabenzotriazol-1-yl)-*N*,*N*,*N'*,*N'*-tetramethyluronium hexafluorophosphate (0.148 mmol) and 64.80 μl of diisopropylethylamine (0.37 mmol) were added to the solution and allowed to react for 30 min at room temperature. Afterward, varying amounts (15, 26.3, or 35 mg) of the peptide NapFFKYp, dissolved in 5 ml of dimethyl sulfoxide, were added dropwise to the above mixture and reacted for 24 hours at 40°C to synthesize HA-NapFFKYp with grafting rates of 14, 20, and 33%, respectively. HA-NapFFKYp was then purified by dialysis.

Characterization of self-assembled HA-NapFFKYp

The self-assembly of HA-NapFFKYp into nanofibrils in the presence of ALP was observed by TEM and SEM. Briefly, ALP (0.1 U/ml) was

added to a 0.1 wt % HA-NapFFKYp solution and reacted for 2 hours at 37°C. For TEM imaging, 3 μl of the solution was deposited onto a copper grid and allowed to dry for 5 min. The sample was stained with 2% uranyl acetate for 15 min and subsequently imaged by TEM (Thermo Fisher Scientific, Talos F200x). A HA-NapFFKYp solution without ALP was used as a control. For SEM imaging, the sample was first freeze dried to obtain a solid product. The dried sample was then mounted on conductive adhesive, coated with gold, and imaged by SEM (ZEISS, Merlin, Germany). To analyze the secondary structure of the self-assembled HA-NapFFKYp, circular dichroism) spectra were recorded. The sample was placed in a 10-mm-pathlength quartz cuvette and scanned for two cycles.

Rheology test
The mechanical properties of the HA-NapFFKY gel were assessed using an AR2000ex rheometer (TA Instruments, US). Briefly, ALP (0.1 U/ml) was added to a 0.1 wt % HA-NapFFKYp solution and incubated for 2 hours at 37°C to form the gel. The storage modulus (G') and loss modulus (G'') of the gel were measured at a frequency of 10.0 Hz and a strain of 1%. A HA-NapFFKYp solution without ALP was used as a control.

Cell lines and cell culture
Rat MSCs derived from bone marrow were purchased from iCell Bioscience Inc. (RAT-iCell-s018). Luciferase-expressing MSCs derived from rat bone marrow were purchased from Nanjing Wanmuchun Biotechnology Co., Ltd. (Nanjing, China). The cells were cultured in Dulbecco's modified Eagle's medium (DMEM) supplemented with 10% fetal bovine serum (FBS) and penicillin-streptomycin (100 IU/ml) at 37°C in a humidified atmosphere containing 5% CO_2 and with 95% relative humidity.

Preparation of pFM-encapsulated individual MSCs
MSCs (2×10^6) suspended in 0.5 ml of HA-NapFFKYp solution were gently agitated for 45 min at room temperature. Unabsorbed HA-NapFFKYp on the MSC surface was removed by centrifugation at 250g for 5 min. Subsequently, the cells were resuspended in 0.5 ml of FBS-free medium containing ALP (0.1 U/ml) and incubated for 2 hours. After incubation, the cells were collected by centrifugation at 250g for 5 min and then immersed twice in 0.5 ml of HA-NapFFKYp solution. Last, cells singly encapsulated in pFM were harvested and washed with 1× PBS via two centrifugation steps.

Characterization of pFM-encapsulated MSCs
To characterize pFM formed on individual MSC surfaces, MSCs were first stained with DiD and then encapsulated with rhodamine B–labeled HA-NapFFKYp using the above method. The resulting HA-NapFFKYp nanofibrils on the MSC surface were further stained with Congo Red. The pFM-MSCs were then analyzed by a BD FACSVerse flow cytometer and imaged with a laser scanning confocal microscope. MSCs treated with rhodamine B–labeled HA and NapFFKYp separately were set as control groups. The surface morphology of native MSCs and pFM-MSCs was directly observed by SEM. MSCs were seeded onto cell slides and encapsulated with HA-NapFFKYp as described above. The slides were rapidly frozen in liquid nitrogen for 5 s and then freeze dried. Last, the samples were gold coated and imaged by SEM.

Cytotoxicity of HA-NapFFKYp
MSCs were seeded in a 96-well plate at a density of 1×10^4 cells per well. After 24 hours of culture, the cells were singly encapsulated with HA-NapFFKYp at varying peptide grafting rates (14, 20, and 33%)

and concentrations (0.25, 0.5, 0.75, and 1%), as described above. Subsequently, 10 μl of CCK-8 solution was added to each well. After an additional 2 hours of incubation, the absorbance was measured at 450 nm.

Mechanical properties of MSCs encapsulated with pFM
MSCs were seeded onto 8-mm cell slides and incubated for 24 hours. Then, different concentrations (0.25, 0.5, 0.75, and 1%) of HA-NapFFKYp with a fixed peptide grafting rate of 20% were used to encapsulate individual MSCs. The mechanical strength of the pFM-MSCs was measured using atomic force microscope (AFM) equipped with a spherical probe with a diameter of 10 μm.

Cytokine release study of MSCs encapsulated with pFM
Different concentrations (0.25, 0.5, 0.75, and 1%) of HA-NapFFKYp with a fixed peptide grafting rate of 20% were used to encapsulate individual MSCs. Subsequently, the resulting pFM-MSCs were seeded into a 12-well plate (3000 cells per well) and cultured in DMEM supplemented with 10% FBS for 24 hours. After that, the medium was replaced with serum-free DMEM, and the cells were incubated for an additional 3 days. Last, the DMEM containing secreted cytokines was collected by centrifugation. The concentrations of various cytokines in the medium were measured using ELISA kits according to the manufacturer's instructions. The ELISA kits were obtained from Shanghai Enzyme-linked Biotechnology Co., Ltd.

Cytoprotective effect of pFM on MSCs
HA-NapFFKYp at a concentration of 0.75% and a peptide grafting rate of 20% was used to encapsulate individual MSCs. For the physical stress test, native MSCs and pFM-MSCs were resuspended in 1× PBS at a density of 1×10^6 cells/ml and centrifuged at different centrifugation speeds (400g, 800g, and 1200g) at 4°C for 5 min. After six rounds of centrifugation, the cells were resuspended in 1 ml of culture medium, and their viability was measured using the CCK-8 assay. For the inflammatory factor, hypoxia, and ROS challenge tests, native MSCs and pFM-MSCs were seeded into a 96-well plate at a density of 1×10^4 cells per well. To assess resistance to inflammatory factors, a culture medium containing various concentrations of TNF-α (50, 75, and 100 ng/ml) was added to each well and incubated for 24 hours. For the hypoxia challenge, a medium containing $Na_2S_2O_4$ at concentrations of 2, 4, and 6 mM was added and incubated for 5 hours. For the ROS challenge, a medium containing H_2O_2 at concentrations of 0.4, 0.8, and 1.2 mM was added and incubated for 2 hours. Last, MSC viability was measured using the CCK-8 assay.

RNA sequencing
Total RNA was extracted from cells using RNAiso Plus (TaKaRa, Japan) according to the manufacturer's protocol. High-throughput RNA sequencing and transcriptome analysis were subsequently performed by LC-BIO Biotech Ltd. (Hangzhou, China). Quantitative gene expression analysis, as well as GO and KEGG pathway enrichment analyses, was conducted using OmicStudio tools (www.omicstudio.cn). A volcano plot and heatmap were generated using R version 4.1.3 on the OmicStudio platform.

Inhibition and activation of the Piezo1 channel
Piezo1-induced calcium influx was inhibited by incubating cells with 2.5 μM GsMTx4 (MedChemExpress, US) for 24 hours at 37°C and 5% CO_2. Activation of Piezo1 was induced by incubating cells with 2.5 μM Yoda1 (MedChemExpress, US) for 12 hours at 37°C and 5% CO_2.

Real-time PCR

Total RNA was extracted from cells using the NumSpin Cell Total RNA Kit (NCM Biotech, China). Subsequently, RNA was reverse transcribed into cDNA using the HiFiScript gDNA Removal RT MasterMix Kit (CWBIO, China). qPCR was then performed using the MagicSYBR Mixture Kit (CWBIO, China) on a LightCycler 96 real-time fluorescence quantitative PCR instrument (Roche, Switzerland). GAPDH was used as a housekeeping gene for normalization. Primers were purchased from IGE Biotech (Guangzhou, China), and the sequences were as follows: rat GAPDH: GGCAAGTTCAACGGCACAG (forward, 5′-3′), CGCCAGTAGACTCCACGACAT (reverse, 5′-3′); rat Piezo1: AGCAAGCAGGCACAAAGGC (forward, 5′-3′), CGCACAAACTT-GCCAACGAC (reverse, 5′-3′); rat Mmp13: AGCAGGTTGAGCCT-GAACTGT (forward, 5′-3′), GCAGCACTGAGCCTTTTCACC (reverse, 5′-3′); rat CD44: CTGCCTCAGCCCACAACAAC (forward, 5′-3′), CGGTCCATGAAACATCCTCTTG (reverse, 5′-3′); rat HMMR: TGCCCTGGATGAGCTGGA (forward, 5′-3′), GCATGTG-CAGCGGTTCTTT (reverse, 5′-3′); rat TLR4: AGCTTTGGT-CAGTTGGCTCT (forward, 5′-3′), CAGGATGACACCATTGAAGC (reverse, 5′-3′); rat Bcl2: TGGGATGCCTTTGTGGAACTAT (forward, 5′-3′), AGAGACAGCCAGGAGAAATCAAAC (reverse, 5′-3′); rat Bax: ATGGAGCTGCAGAGGATGA (forward, 5′-3′), CCAGTTT-GCTAGCAAAGTAG (reverse, 5′-3′).

Small interfering RNA transfection

The Mmp13 small interfering RNA was designed and synthesized by GenScript (Nanjing, China). Cells were transfected in six-well plates at a density of 1×10^5 cells per well for 48 hours using a transfection kit (Thermo Fisher Scientific). After transfection, cells were cultured at 37°C with 5% CO_2.

Calcium measurements

Intracellular Ca^{2+} was visualized using the calcium probe Fluo-4-AM (Beyotime, China). Briefly, 12 hours after encapsulation, MSCs were incubated with Fluo-4-AM (2.5 μM) for 30 min in the dark at 37°C, followed by imaging using a laser scanning confocal microscope. Ca^{2+} levels were quantified using ImageJ software.

Western blotting

Cells were lysed using radioimmunoprecipitation assay buffer to extract proteins. The samples were separated by SDS–polyacrylamide gel electrophoresis for 90 min and then transferred to polyvinylidene difluoride membranes by wet transfer. The membranes were blocked with 5% skim milk for 2 hours, followed by overnight incubation at 4°C with primary antibodies: anti-MMP13 (1:3000, ab39012, Abcam, UK), anti–Phospho-Akt (1:2000, 4060, CST, US), anti-AKT (1:1000, 4691, CST, US), and anti-GAPDH (1:50,000, 60004-1-Ig, Proteintech, China). Afterward, the membranes were incubated with horseradish peroxidase–conjugated secondary antibodies, and target bands were visualized using the ChemiDoc Touch system (Bio-Rad, US).

Ponceau S staining of collagen

Three-dimensional collagen scaffolds were prepared in 48-well plates using collagen I (Gibco, US) and cocultured with pFM-MSCs for 24 hours, followed by fixation with 2.5% glutaraldehyde for 30 min. The glutaraldehyde fixative was carefully removed using 1× PBS, and the samples were subsequently stained with 0.2% Ponceau S red for 30 min. After staining, the samples were washed three times with deionized water to remove any excess dye.

Animals

All animal experimental procedures were approved by the Animal Care and Use Committee of South China University of Technology (2023103). Sprague-Dawley rats (males, 250 g each) were purchased from Hunan SJA Laboratory Animal Co., Ltd. The rats were housed in pathogen-free facilities, maintained on a 12-hour light/dark cycle, and kept at a controlled temperature of 22°C with a humidity range of 45–60%.

Establishment of rats MI model and treatment

MI surgery was performed on Sprague-Dawley rats following a previously established method with some modifications. Briefly, the rats were anesthetized via intraperitoneal injection of 10% chloral hydrate at a dose of 350 mg/kg. Following anesthesia, the rats were secured on a heating pad maintained at 37°C in a supine position. They were then ventilated with a small animal ventilator set to 80 breaths per minute and a tidal volume of 6.0 ml. The left chest was opened to expose the heart. Subsequently, the left anterior descending coronary artery (LAD) was permanently ligated using a 7-0 silk suture at a site about 3 mm from its origin. Myocardial ischemia was confirmed by the observation of myocardial blanching. Immediately, 1×10^6 native MSCs, pFM-MSCs in 100 μl of PBS, or PBS alone was delivered intramyocardially via a five-point injection at the border of the infarct zone. Last, the open chest cavity was closed, and air was evacuated to prevent pneumothorax. Transthoracic echocardiography was performed using the Vevo F2 Imaging System (FUJI-FILM VisualSonics Inc., Canada). After 28 days, the heart function of the different groups was assessed in the different groups. Animals were lightly anesthetized in a chamber using isoflurane. The rats were positioned supine on the echo platform, and their limbs were secured. Thereafter, the rats were anesthetized by inhaling isoflurane mixed with O_2 to stabilize the heart rate at ~300 to 500 beats per minute, and both M-mode echocardiography and B-mode echocardiography were performed. The cardiac parameters, LVEF and LVFS, were obtained by measuring the long axis and short axis.

Bioluminescence imaging detection

The method for inducing MI surgery and administering MSC injection was the same as described above. MSCs engineered to express luciferase were used in the experiment. On days 1, 3, 5, and 7, the rats were anesthetized with 10% chloral hydrate (350 mg/kg) and intraperitoneally administered D-luciferin (150 mg/kg in PBS, Aladdin). Following the injection, bioluminescence images were captured over a 5-min period using an IVIS Lumina Series III System (PerkinElmer).

Cardiac PET/CT imaging

The method for inducing MI surgery and performing MSC injection was consistent with the aforementioned procedure. Sprague-Dawley rats were subjected to a 24-hour fasting period before image acquisition. On days 7, 14, and 28, PET acquisition was conducted using a nanoScan PET/CT system (InViscan Imaging Systems). The rats were anesthetized using 2.5% isoflurane administered in oxygen. A dose of 20 MBq (megabecquerels) of ^{18}F-FAPI was introduced into ~300 μl of normal saline and subsequently injected into the rats via the tail vein. After a 30-min interval, a 10-min dynamic acquisition commenced without delay. To facilitate attenuation correction and provide an anatomical reference, CT images were acquired following PET imaging. The rats were administered 2.5% isoflurane in oxygen throughout the scan and were maintained at 37°C.

Quantification of hydroxyproline

A hydroxyproline assay kit (Sangon, D799573-0050) was used to quantify hydroxyproline. Approximately 0.1 g of heart tissue from each rat was weighed and homogenized in 1 ml of 6 M HCl, followed by heating at 110°C until no large clumps remained. The lysate was then centrifuged at 16,000 rpm and 25°C for 20 min, and the pH was adjusted to 6 to 8 using 10 M NaOH (~1.5 ml). Subsequently, 100 μl of chloramine T oxidative buffer was added to 100 μl of lysate and incubated at room temperature for 20 min. Afterward, 100 μl of 4-(dimethylamino)benzaldehyde was added to the lysate and incubated for 20 min at 60°C, followed by 15 min at room temperature. Colorimetric signals were recorded at an absorbance of 560 nm using a plate reader. The concentration of hydroxyproline was determined using the standard curve.

Quantification of heart tissue microelasticity

After perfusion of the hearts with PBS, the heart tissues were embedded in optimal cutting temperature compound. The hearts were then frozen using dry ice and stored at −80°C for no more than 1 week. The tissues were sectioned into 15-μm-thick slices and stored at −20°C for no more than 24 hours before analysis. After rinsing the thawed tissue sections with PBS, atomic force microscopy using a silicon nitride cantilever with an 18° pyramidal tip was performed to measure tissue microelasticity. A force set point of 250 nm and a tip velocity of 0.5 μm/s were applied until a trigger voltage of 0.5 V was reached.

Histological analysis

On day 28, all animals were anesthetized and then euthanized. The hearts were excised and fixed with 4% paraformaldehyde for more than 24 hours. The heart tissues were dehydrated using a graded ethanol series, embedded in paraffin, and sectioned into 5-μm-thick slices for Masson's trichrome, Sirius Red, and H&E staining according to standard protocols. In addition, heart tissues were embedded in optimal cutting temperature compound and cryosectioned into 10-μm-thick slices for immunofluorescence staining. Specifically, the cryosections were first permeabilized with 0.2% Triton X-100 and then blocked with 5% bovine serum albumin to reduce nonspecific binding, followed by incubation with primary antibodies against CD31 and α-SMA at 4°C overnight. On the following day, the sections were washed three times with PBS and incubated with Alexa Fluor 488–, Cy3-, or Cy5-conjugated secondary antibodies for 2 hours at room temperature. Last, the sections were stained with DAPI (4′,6-diamidino-2-phenylindole) and imaged using a laser scanning confocal microscope.

Statistical analysis

All data are presented as the means ± standard deviation (SD). Statistical analyses were performed using GraphPad Prism 8. Comparisons between two groups were conducted using an unpaired Student's t test, while comparisons among multiple groups were performed using a one-way analysis of variance (ANOVA). $P < 0.05$ was considered statistically significant.

Supplementary Materials

This PDF file includes:
Figs. S1 to S24

REFERENCES

1. N. C. Henderson, F. Rieder, T. A. Wynn, Fibrosis: From mechanisms to medicines. *Nature* **587**, 555–566 (2020).
2. J. Herrera, C. A. Henke, P. B. Bitterman, Extracellular matrix as a driver of progressive fibrosis. *J. Clin. Invest.* **128**, 45–53 (2018).
3. B. López, S. Ravassa, M. U. Moreno, G. S. José, A. Beaumont, A. González, J. Díez, Diffuse myocardial fibrosis: Mechanisms, diagnosis and therapeutic approaches. *Nat. Rev. Cardiol.* **18**, 479–498 (2021).
4. H. Zhang, P. N. Thai, R. V. Shivnaraine, L. Ren, X. Wu, D. H. Siepe, Y. Liu, C. Tu, H. S. Shin, A. Caudal, S. Mukherjee, J. Leitz, W. T. L. Wen, W. Liu, W. Zhu, N. Chiamvimonvat, J. C. Wu, Multiscale drug screening for cardiac fibrosis identifies MD2 as a therapeutic target. *Cell* **187**, 7143–7163.e22 (2024).
5. S. Mendis, I. Graham, J. Narula, Addressing the global burden of cardiovascular diseases; need for scalable and sustainable frameworks. *Glob. Heart* **17**, 48 (2022).
6. N. Srour, B. Thébaud, Mesenchymal stromal cells in animal bleomycin pulmonary fibrosis models: A systematic review. *Stem Cells Transl. Med.* **4**, 1500–1510 (2015).
7. H. Bao, M. Wu, J. Xing, Z. Li, Y. Zhang, A. Wu, J. Li, Enzyme-like nanoparticle–engineered mesenchymal stem cell secreting HGF promotes visualized therapy for idiopathic pulmonary fibrosis in vivo. *Sci. Adv.* **10**, eadq0703 (2024).
8. X. Wu, J. Jiang, Z. Gu, J. Zhang, Y. Chen, X. Liu, Mesenchymal stromal cell therapies: Immunomodulatory properties and clinical progress. *Stem Cell Res. Ther.* **11**, 345 (2020).
9. T. P. Lozito, W. M. Jackson, L. J. Nesti, R. S. Tuan, Human mesenchymal stem cells generate a distinct pericellular zone of MMP activities via binding of MMPs and secretion of high levels of TIMPs. *Matrix Biol.* **34**, 132–143 (2014).
10. O. Levy, R. Kuai, E. M. J. Siren, D. Bhere, Y. Milton, N. Nissar, M. de Biasio, M. Heinelt, B. Reeve, R. Abdi, M. Alturki, M. Fallatah, A. Almalik, A. H. Alhasan, K. Shah, J. M. Karp, Shattering barriers toward clinically meaningful MSC therapies. *Sci. Adv.* **6**, eaba6884 (2020).
11. P. K. Nguyen, E. Neofytou, J.-W. Rhee, J. C. Wu, Potential strategies to address the major clinical barriers facing stem cell regenerative therapy for cardiovascular disease: A review. *JAMA Cardiol.* **1**, 953–962 (2016).
12. G. Orive, E. Santos, D. Poncelet, R. M. Hernández, J. L. Pedraz, L. U. Wahlberg, P. de Vos, D. Emerich, Cell encapsulation: Technical and clinical advances. *Trends Pharmacol. Sci.* **36**, 537–546 (2015).
13. H. Xing, H. Lee, L. Luo, T. R. Kyriakides, Extracellular matrix-derived biomaterials in engineering cell function. *Biotechnol. Adv.* **42**, 107421 (2020).
14. S. Liu, J. M. Yu, Y. C. Gan, X. Z. Qiu, Z. C. Gao, H. Wang, S. X. Chen, Y. Xiong, G. H. Liu, S. E. Lin, A. McCarthy, J. V. John, D. X. Wei, H. H. Hou, Biomimetic natural biomaterials for tissue engineering and regenerative medicine: New biosynthesis methods, recent advances, and emerging applications. *Mil. Med. Res.* **10**, 16 (2023).
15. J. Nicolas, S. Magli, L. Rabbachin, S. Sampaolesi, F. Nicotra, L. Russo, 3D extracellular matrix mimics: Fundamental concepts and role of materials chemistry to influence stem cell fate. *Biomacromolecules* **21**, 1968–1994 (2020).
16. M. E. Wechsler, V. V. Rao, A. N. Borelli, K. S. Anseth, Engineering the MSC secretome: A hydrogel focused approach. *Adv. Healthc. Mater.* **10**, e2001948 (2021).
17. O. Chaudhuri, J. Cooper-White, P. A. Janmey, D. J. Mooney, V. B. Shenoy, Effects of extracellular matrix viscoelasticity on cellular behaviour. *Nature* **584**, 535–546 (2020).
18. A. Mishra, U. Modi, R. Sharma, D. Bhatia, R. Solanki, Biochemical and biophysical cues of the extracellular matrix modulates stem cell fate: Progress and prospect in extracellular matrix mimicking biomaterials. *Biomed. Eng. Adv.* **9**, 100143 (2025).
19. M. Rodrigues, N. Kosaric, C. A. Bonham, G. C. Gurtner, Wound healing: A cellular perspective. *Physiol. Rev.* **99**, 665–706 (2019).
20. F. Qu, F. Guilak, R. L. Mauck, Cell migration: Implications for repair and regeneration in joint disease. *Nat. Rev. Rheumatol.* **15**, 167–179 (2019).
21. L. Zhu, L. Liu, A. Wang, J. Liu, X. Huang, T. Zan, Positive feedback loops between fibroblasts and the mechanical environment contribute to dermal fibrosis. *Matrix Biol.* **121**, 1–21 (2023).
22. H.-M. Chuang, Y.-S. Chen, H.-J. Harn, The versatile role of matrix metalloproteinase for the diverse results of fibrosis treatment. *Molecules* **24**, 4188 (2019).
23. M. Xue, C. J. Jackson, Extracellular matrix reorganization during wound healing and its impact on abnormal scarring. *Adv. Wound Care* **4**, 119–136 (2015).
24. J. Zhou, X. Du, Y. Gao, J. Shi, B. Xu, Aromatic-aromatic interactions enhance interfiber contacts for enzymatic formation of a spontaneously aligned supramolecular hydrogel. *J. Am. Chem. Soc.* **136**, 2970–2973 (2014).
25. Z. M. Yang, G. L. Liang, B. Xu, Enzymatic hydrogelation of small molecules. *Acc. Chem. Res.* **41**, 315–326 (2008).
26. A. V. Persikov, B. Brodsky, Unstable molecules form stable tissues. *Proc. Natl. Acad. Sci. U.S.A.* **99**, 1101–1103 (2002).
27. S. Sen, J. Xavier, N. Kumar, M. Z. Ahmad, O. P. Ranjan, Exosomes as natural nanocarrier-based drug delivery system: Recent insights and future perspectives. *3 Biotech* **13**, 101 (2023).
28. B. Zhou, K. Xu, X. Zheng, T. Chen, J. Wang, Y. Song, Y. Shao, S. Zheng, Application of exosomes as liquid biopsy in clinical diagnosis. *Signal Transduct. Target. Ther.* **5**, 144 (2020).
29. L. Zhang, G. Liu, K. Lv, J. Xin, Y. Wang, J. Zhao, W. Hu, C. Xiao, K. Zhu, L. Zhu, J. Nan, Y. Feng, H. Zhu, W. Chen, W. Zhu, J. Zhang, J. Wang, B. Wang, X. Hu, Surface-anchored nanogel coating endows stem cells with stress resistance and reparative potency via turning down the cytokine-receptor binding pathways. *Adv. Sci.* **8**, 2003348 (2021).

30. H. M. Micek, N. Yang, M. Dutta, L. Rosenstock, Y. Ma, C. Hielsberg, M. McCord, J. Notbohm, S. McGregor, P. K. Kreeger, The role of Piezo1 mechanotransduction in high-grade serous ovarian cancer: Insights from an in vitro model of collective detachment. *Sci. Adv.* **10**, eadl4463 (2024).

31. W. Morozumi, K. Aoshima, S. Inagaki, Y. Iwata, Y. Takagi, S. Nakamura, H. Hara, M. Shimazawa, Piezo1 activation induces fibronectin reduction and PGF2α secretion via arachidonic acid cascade. *Exp. Eye Res.* **215**, 108917 (2022).

32. H. Kang, Z. Hong, M. Zhong, J. Klomp, K. J. Bayless, D. Mehta, A. V. Karginov, G. Hu, A. B. Malik, Piezo1 mediates angiogenesis through activation of MT1-MMP signaling. *Am. J. Physiol. Cell Physiol.* **316**, C92–C103 (2019).

33. M. J. Li, C. X. Li, J. Y. Li, Z. C. Gong, B. Shao, Y. C. Zhou, Y. J. Xu, M. Y. Jia, Biomechanism of abnormal stress on promoting osteoarthritis of temporomandibular joint through Piezo1 ion channel. *J. Oral Rehabil.* **51**, 1935–1946 (2024).

34. P. Qiao, Y. Wang, K. Zhu, D. Zheng, Y. Song, D. Jiang, C. Qin, X. Lan, Noninvasive monitoring of reparative fibrosis after myocardial infarction in rats using ^{68}Ga-FAPI-04 PET/CT. *Mol. Pharm.* **19**, 4171–4178 (2022).

35. S. Hinderer, K. Schenke-Layland, Cardiac fibrosis—A short review of causes and therapeutic strategies. *Adv. Drug Deliv. Rev.* **146**, 77–82 (2019).

36. W. C. Parks, C. L. Wilson, Y. S. López-Boado, Matrix metalloproteinases as modulators of inflammation and innate immunity. *Nat. Rev. Immunol.* **4**, 617–629 (2004).

37. A. M. Manicone, J. K. McGuire, Matrix metalloproteinases as modulators of inflammation. *Semin. Cell Dev. Biol.* **19**, 34–41 (2008).

38. X. Zhao, J. Chen, H. Sun, Y. Zhang, D. Zou, New insights into fibrosis from the ECM degradation perspective: The macrophage-MMP-ECM interaction. *Cell Biosci.* **12**, 117 (2022).

39. K. Chen, M. Xu, F. Lu, Y. He, Development of matrix metalloproteinases-mediated extracellular matrix remodeling in regenerative medicine: A mini review. *Tissue Eng. Regener. Med.* **20**, 661–670 (2023).

40. Y. Ling, J. Rubin, Y. Deng, C. Huang, U. Demirci, J. M. Karp, A. Khademhosseini, A cell-laden microfluidic hydrogel. *Lab Chip* **7**, 756–762 (2007).

41. T. Kamperman, M. Karperien, S. Le Gac, J. Leijten, Single-cell microgels: Technology, challenges, and applications. *Trends Biotechnol.* **36**, 850–865 (2018).

42. A. S. Mao, J. W. Shin, S. Utech, H. Wang, O. Uzun, W. Li, M. Cooper, Y. Hu, L. Zhang, D. A. Weitz, D. J. Mooney, Deterministic encapsulation of single cells in thin tunable microgels for niche modelling and therapeutic delivery. *Nat. Mater.* **16**, 236–243 (2017).

43. S. W. Wong, C. R. Tamatam, I. S. Cho, P. T. Toth, R. Bargi, P. Belvitch, J. C. Lee, J. Rehman, S. P. Reddy, J. W. Shin, Inhibition of aberrant tissue remodelling by mesenchymal stromal cells singly coated with soft gels presenting defined chemomechanical cues. *Nat. Biomed. Eng.* **6**, 54–66 (2022).

44. J. J. Schmidt, J. Jeong, H. Kong, The interplay between cell adhesion cues and curvature of cell adherent alginate microgels in multipotent stem cell culture. *Tissue Eng. Part A* **17**, 2687–2694 (2011).

45. A. H. Lewis, J. Grandl, Mechanical sensitivity of Piezo1 ion channels can be tuned by cellular membrane tension. *eLife* **4**, e12088 (2015).

46. I. Lüchtefeld, I. V. Pivkin, L. Gardini, E. Zare-Eelanjegh, C. Gäbelein, S. J. Ihle, A. M. Reichmuth, M. Capitanio, B. Martinac, T. Zambelli, M. Vassalli, Dissecting cell membrane tension dynamics and its effect on Piezo1-mediated cellular mechanosensitivity using force-controlled nanopipettes. *Nat. Methods* **21**, 1063–1073 (2024).

47. M. Wang, S. Sun, G. Dong, F. Long, J. T. Butcher, Soft, strong, tough, and durable protein-based fiber hydrogels. *Proc. Natl. Acad. Sci. U.S.A.* **120**, e2213030120 (2023).

48. N. Shembekar, C. Chaipan, R. Utharala, C. A. Merten, Droplet-based microfluidics in drug discovery, transcriptomics and high-throughput molecular genetics. *Lab Chip* **16**, 1314–1331 (2016).

49. H. Soleymani, M. Ghorbani, M. Sedghi, A. Allahverdi, H. Naderi-Manesh, Microfluidics single-cell encapsulation reveals that poly-l-lysine-mediated stem cell adhesion to alginate microgels is crucial for cell-cell crosstalk and its self-renewal. *Int. J. Biol. Macromol.* **274**, 133418 (2024).